

Gravity and magma induced spreading of Mount Etna volcano revealed by satellite radar interferometry

P. Lundgren

Jet Propulsion Laboratory, California Institute of Technology, Pasadena, California, USA

F. Casu, M. Manzo, A. Pepe, P. Berardino, E. Sansosti, and R. Lanari

Istituto per il Rilevamento Elettromagnetico dell'Ambiente, Consiglio Nazionale delle Ricerche, Napoli, Italy

Received 29 September 2003; revised 20 November 2003; accepted 19 December 2003; published 17 February 2004.

[1] Mount Etna underwent a cycle of eruptive activity over the past ten years. Here we compute ground displacement maps and deformation time series from more than 400 radar interferograms to reveal Mount Etna's average and time varying surface deformation from 1992 to 2001. We find that during this time interval it experienced magmatic inflation and radial spreading to the West, South, and East. Steady relative motion between the West and South flanks, and between the East and North flanks, during this time interval, suggests they are related to gravitational spreading of the volcanic edifice. Time series analysis shows that growth of a southeastern basal anticline began with the end of magma recharge in 1995, thus showing a direct link between deep-seated magma intrusions and edifice spreading. These observations support a complex mode of radial gravitational collapse underlain by deeper magma driven basal spreading, although ultimately the two must be related. **INDEX TERMS:** 1243 Geodesy and Gravity: Space geodetic surveys; 8494 Volcanology: Instruments and techniques; 8499 Volcanology: General or miscellaneous. **Citation:** Lundgren, P., F. Casu, M. Manzo, A. Pepe, P. Berardino, E. Sansosti, and R. Lanari (2004), Gravity and magma induced spreading of Mount Etna volcano revealed by satellite radar interferometry, *Geophys. Res. Lett.*, 31, L04602, doi:10.1029/2003GL018736.

1. Introduction

[2] Mt. Etna is a large, highly active volcano that is structurally complex (Figure 1). It features two well-developed rift systems extending to the north and south from the summit craters through a series of fault systems as its eastern and southern flanks move away from the volcano's center [*Rust and Neri*, 1996; *Borgia et al.*, 1992, 2000; *Froger et al.*, 2001]. However, fundamental questions remain regarding the structures and dynamics of this flank motion, with models ranging from shallow, gravity driven edifice spreading [*Lo Giudice and Rasà*, 1992; *McGuire et al.*, 1997], to deeper seated magmatic intrusion driven spreading [*Borgia et al.*, 1992, 2000; *Lundgren et al.*, 2003; *Bonforte and Puglisi*, 2003], or possibly both [*Rust and Neri*, 1996; *Tibaldi and Groppelli*, 2002]. This spreading has generally been viewed as occurring across its eastern and southern flanks, from the Pernicana fault to the NE to the Ragalna fault to the SW. However, the south and east flanks of Etna do not form a single block, with

differential motion occurring in several places, most notably across the Trecastagni-Mascalucia fault system that separates the southern flank (culminating in the southern anticline) from the eastern flank [*Lo Giudice and Rasà*, 1992].

[3] Volcano spreading can be viewed as one single process, with laboratory experiments requiring a horizontal low-viscosity substratum to accommodate basal spreading, which then leads to edifice faulting [*Merle and Borgia*, 1996]. The InSAR data presented here, provide one of the most spatially and temporally complete sets of observations and show that both upper edifice collapse (gravity driven) and deeper seated (possibly driven by magma pressure increases) basal spreading must be present.

2. InSAR Analysis

[4] Interferometric synthetic aperture radar (InSAR) is a technique for detecting centimeter level surface displacements at 50–100 m sampling over ~100 km spatial scales [*Rosen et al.*, 2000]. More than 400 interferograms with perpendicular baselines less than 160 m over both short and long time intervals demonstrate structural (fault bounded flank) and magma (inflation/deflation) related deformation, as well as differing levels of atmospheric noise (Figures A1–A22¹). Long time-span interferograms of Mt. Etna from both ascending and descending passes of the European Space Agency's ERS-1 and ERS-2 satellites (Figure 2) following termination of the flank eruption in March 1993, reveal the complex ground deformation that occurred during the period of recharge of the volcanic plumbing system [*Lanari et al.*, 1998; *Lundgren et al.*, 2003] and subsequent summit activity [*Patanè et al.*, 2003]. The InSAR patterns reveal expansion of the ground surface due to pressure increase in the magma system. The asymmetry of the roughly concentric bands in the ascending and descending interferograms is related to the projection of the horizontal and vertical surface displacements into the radar line-of-sight [*Lundgren et al.*, 2003]. Linear to arcuate surface offsets reveal active fault traces that serve to accommodate relative motions of its flanks [*Borgia et al.*, 2000; *Froger et al.*, 2001]. The crossing fault systems of the Ragalna and Southwest radial fault system support the radial spreading models of *Merle and Borgia* [1996].

[5] To reconstruct the temporal evolution of Etna's surface deformation we invert a large number of interferograms (Tables A1 and A2¹) to derive an InSAR time series

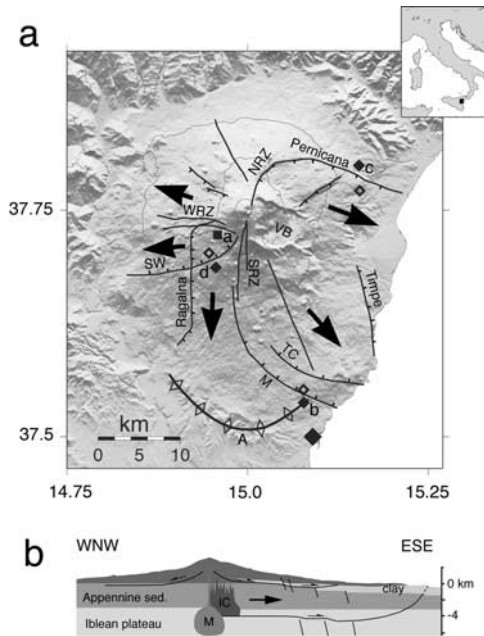


Figure 1. (a) Shaded relief map of Mt. Etna showing its main faults and rift zones, inset in upper right shows location of study area in eastern Sicily (Italy). Black arrows show general sense of flank motion. Black lines show rift zones and faults. Tick marks indicate normal motion with ticks on the hanging wall. TC is the Trecastagni fault; M is the Mascalucia fault system; SW is the Southwest fault system; WRZ, NRZ, SRZ indicate the Western, North-eastern, and Southern rift zones, respectively. 'A' indicates the anticline crest at the toe of the southern flank. VB is the Valle del Bove. The large solid diamond southeast of the anticline indicates the reference point for the velocity maps shown in Figure 3. The solid square south of the WRZ and labeled 'a' is the point used in Figure 4a. Solid and open diamonds adjacent the Mascalucia/anticline, 'b', Pernicana, 'c', and SW, 'd', faults show the locations for the time series displacements shown in Figures 4b, 4c, and 4d, respectively; with displacements calculated as the difference (solid-open). (b) Structural cross section (through the summit) of Mt. Etna. To the right of the summit structures are based on *Tibaldi and Groppelli* [2002] interpretation. M is the magma body, IC the intrusive complex, and 'clay' the sub-Etnean clay layer. To the left (west) shallow flank fault is interpreted from this study.

[Lundgren *et al.*, 2001; Berardino *et al.*, 2002]. The algorithm we use is referred to as the small baselines subset (SBAS) technique [Berardino *et al.*, 2002]. It relies on the use of small baseline (less than 160 m perpendicular orbit separation, and 4 years temporal) differential SAR interferograms and on the application of the singular value decomposition (SVD) method; the former allows us to mitigate decorrelation, the latter to link independent SAR acquisition data sets separated by large spatial baselines, thus increasing the number of data used for the analysis. In order to mitigate the effect of the atmospheric artifacts, a filtering operation is performed. This step is based on the observation that the atmospheric signal phase component is highly correlated in space but poorly in time [Ferretti *et al.*, 2000; Hanssen,

2001]. Accordingly, the undesired atmospheric phase signal is estimated as follows: first of all, we remove the temporal low pass component of the deformation signal; then the cascade of a lowpass filtering step in the two-dimensional spatial domain and a temporal highpass filtering operation is performed [Berardino *et al.*, 2002]. In summary, the SBAS approach permits us not only to estimate the mean velocity of the ground deformation, but also to follow its temporal evolution.

3. Results

[6] InSAR time series analysis yields several important results. The average surface velocities (Figure 3) for either the ascending (Figure 3a) or descending (Figure 3b) time series reveal patterns similar to the long time interval interferograms (Figure 2). The difference of the two velocity maps effectively eliminates their vertical and north velocity vectors, and shows surface velocities in the West-East direction (Figure 3c). For these data the heading directions of the ascending and descending ERS satellite tracks are within 0.05° of symmetry and the surface incidence angles are within a few degrees of each other, implying a deviation of less than 3% from West–East horizontal motion. In contrast, their sum gives a picture that is mostly vertical motion (Figure 3d). In this case only the W-E horizontal

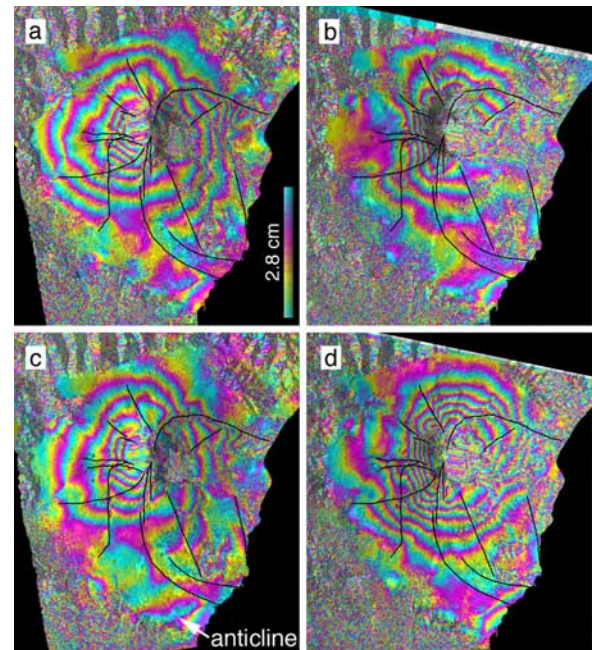


Figure 2. Differential synthetic aperture radar (SAR) interferograms spanning approximately 6 year time intervals from different starting and ending dates since 1993 using European Space Agency ERS-1 and ERS-2 SAR data. Interferograms on the left (a, c) are from ascending satellite passes (radar looks to ENE), while those on the right (b, d) are from descending satellite passes (radar looks to the WNW). (a) Interferogram from 30 May 1993 to 11 Aug. 1999. (b) From 06 June 1993 to 01 Dec. 1999. (c) From 17 Oct. 1993 to 19 Oct. 1999. (d) From 19 Sep. 1993 to 21 Sep. 1999. Solid lines indicate faults and rift zones shown in Figure 1. Observed anticline growth is indicated in (c).

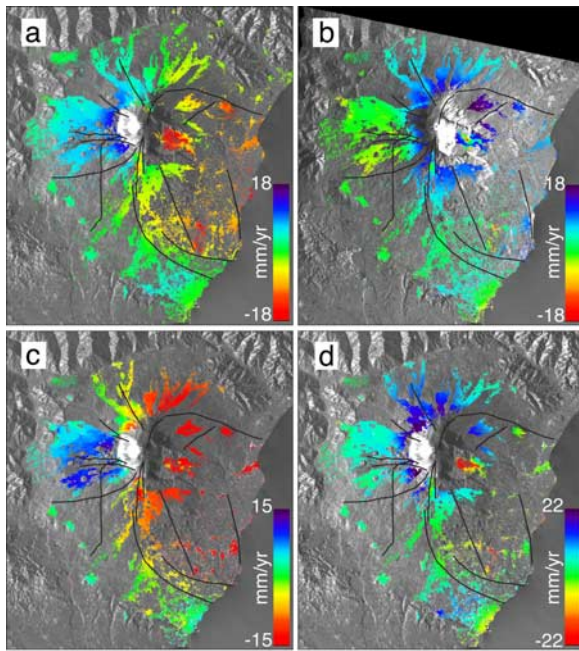


Figure 3. Time series inversion velocity maps. Average linear velocities for each pixel are shown with an average coherence greater than or equal to 0.6, following the analysis technique of *Berardino et al.* [2002]. Zero velocity is referenced to a point indicated by the large solid diamond in Figure 1. (a) Velocities for the ascending ERS satellite track 129, frame 0747. (b) Velocities for the descending track 222, frame 2853. (c) Difference between the ascending and descending velocity maps for pixels in common. (d) Sum of the ascending and descending velocity maps. Solid lines indicate faults shown in Figure 1.

components cancel, with the North and vertical adding. However, due to the high satellite trajectory and steep incidence angle, the contribution from the North horizontal component is less than 10%. The latter confirms the dominantly vertical motion of lava flow compaction in the Valle del Bove, local subsidence at several points on the eastern flank of Mt. Etna, and anticline growth north of Catania. The W-E horizontal and vertical velocity maps show several processes: 1) motion across the southern and eastern flanks is partitioned among transtensional faults (Trecastagni-Mascalucia, Ragalna) [*Borgia et al.*, 2000; *Froger et al.*, 2001]; 2) motion of the western flank toward the West demonstrates that the type of western flank motion observed during the 2001 flank eruption also occurred before 2001; 3) the summit region, including the northern and northeastern upper flanks of Mt. Etna experienced significant uplift, consistent with inflation of the volcano. Long time span interferograms illustrate various modes of deformation, including large-scale inflation, anticline growth, conjugate fault slip, and motions of portions of all the flanks of Mt. Etna (Figure 2). The triangular outer horst on its southwest flank bounded by the Ragalna and SW fault systems had been suggested as an analog to volcano spreading experiments [*Merle and Borgia*, 1996; *Rust and Neri*, 1996] but their continuation into the upper flanks has never been reported. Together with the westward motion of the West flank, these observations agree with the

symmetric spreading model for the 2001 eruption [*Lundgren and Rosen*, 2003], and show that spreading of Mount Etna is not limited to its eastern and southern flanks. Additional examples of differential motion across the SW fault system can be seen in individual interferograms in Figures A18a–A18j, and isolated surface deformation (similar to the 2001 flank motion but on a reduced scale) can be seen in Figure A18k, A18n, A19l, A19m, A19o, A19q, A20c, A20e, A20f, A21e, and A21n.

[7] Time varying ground deformation shows that recharge of the magmatic system and flank motion were linked during this time period (Figure 4). Motion of the summit follows the predominately deflationary/inflationary signal accompanying the 1991–1993 flank eruption, the subsequent recharge of the magma system causing relative inflation from 1993–1995, followed by episodic inflationary and deflationary events superimposed on the general trend of relatively minimal net inflation following 1995 (Figure 4a). Significant relative motion of the southeast anticline (Figure 4b) does not begin until 1995. Faster, more constant motion is found for the Pernicana (Figure 4c) and SW flank fault systems (Figure 4d). The Pernicana fault is well recognized as accommodating significant displacements [*Tibaldi and Groppelli*, 2002]. The Ragalna and SW fault systems are more complex, with relative motion that is comparable to that across the Pernicana fault.

4. Discussion and Conclusions

[8] Despite the complex superposition of magmatic inflationary and flank structural sources to the deformation signal during the 1992 to 2001 time period, the basic observations of radial spreading and anticline motion linked to recharge of the magmatic system derive directly from the data. The observations of west-flank motion and the crossing faults of the Ragalna and Southwest flank systems form

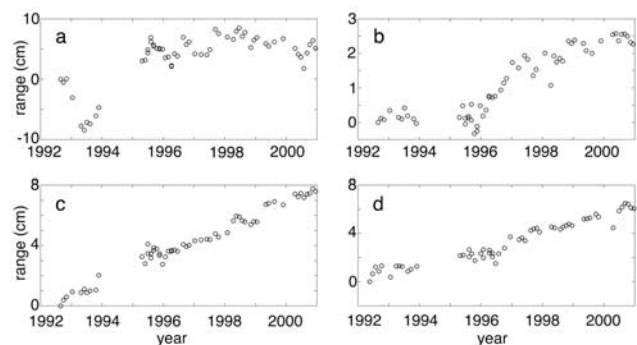


Figure 4. InSAR time series inversion solutions for selected locations shown in Figure 1. Line of sight (satellite range) displacements in panels (a–c) are from the ascending time series, while panel (d) is from the descending time series solution. (a) Motion of the area of maximum deflation/inflation, showing the deflation accompanying the flank eruption that ended in 1993, and the subsequent rapid inflation and period of summit activity from late 1995 to 2001. (b) Relative motion across the Trecastagni-Mascalucia fault and the anticline on the SE flank of Mt. Etna. (c) Relative motion across the Pernicana fault. (d) Relative motion across the SW flank fault system.

the types of flank structures predicted by laboratory models of volcano spreading [Merle and Borgia, 1996]. The significant amount of spreading toward the west is surprising given the assumed buttressing effect of the interior mountains of Sicily. The relatively steady velocities across both the Pernicana (Figure 4c) and SW flank faults (Figure 4d) would support models for shallower 'gravity driven' spreading within the volcanic edifice as controlling their motion, at least within the middle to upper flanks. The observation that anticline growth initiated with the inflation of Mt. Etna, on the other hand, supports models of volcano spreading driven by deeper magma injection at a depth of approximately 5 km below sea level, the modeled source depth of magmatic inflation during the 1993–1995 recharge [Lundgren et al., 2003; Patanè et al., 2003], and lateral displacement of its eastern and southern flanks. In the laboratory models of Merle and Borgia [1996] the deep spreading over the basal decollement and normal faults within the edifice were both continuous with time, with the entire process being governed by basal sliding. However, the observation of relative motion between the southern East flank and the SE anticline suggests that this external, presumably deeper seated motion is less steady and tied to the dynamics of the magma reservoir. It is this difference between anticline growth, by definition representing the deepest levels of the spreading edifice, and the apparent steady motion of the upper flank faults that suggests that the latter are gravity driven. The continuously sliding structures presumably lie at a level that is above the primary upper crustal magma reservoir.

[9] This study shows that the complexity of Mt. Etna's deformation both spatially and temporally requires a more sophisticated and comprehensive model for volcano spreading, highlighting the possible coexistence of both gravity and magma forcing. Future assessments of volcanic hazard posed by flank instabilities and sector collapse must consider both mechanisms.

[10] **Acknowledgments.** ERS raw SAR data were provided by the European Space Agency. This work has been partially supported by the Italian Space Agency and by the Italian National Group of Volcanology (GNV). The precise ERS-1/2 satellite orbit state vectors have been provided by the University of Delft, The Netherlands. The digital elevation model was from the NASA SRTM mission. The authors would like to thank S. Guarino, M. Manunta and G. Zeni for their help. We thank two anonymous reviewers for their insightful comments. Part of this research was carried out at the Jet Propulsion Laboratory, California Institute of Technology, under a contract with the National Aeronautics and Space Administration.

References

Berardino, P., G. Fornaro, R. Lanari, and E. Sansosti (2002), A new algorithm for surface deformation monitoring based on small baseline differ-

- ential SAR interferograms, *IEEE Trans. Geosci. Remote Sens.*, **40**, 2375–2383.
- Bonforte, A., and G. Puglisi (2003), Magma uprising and flank dynamics on Mount Etna volcano, studied using GPS data (1994–1995), *J. Geophys. Res.*, **108**(B3), 2153, doi:10.1029/2002JB001845.
- Borgia, A., L. Ferrari, and G. Pasquare (1992), Importance of gravitational spreading in the tectonic and volcanic evolution of Mount Etna, *Nature*, **357**, 231–235.
- Borgia, A., R. Lanari, E. Sansosti, M. Tesauro, P. Bernardino, G. Fornaro, M. Neri, and J. B. Murray (2000), Actively growing anticlines beneath Catania from the distal motion of Mount Etna's decollement measured by SAR interferometry and GPS, *Geophys. Res. Lett.*, **27**, 3409–3412.
- Ferretti, A., C. Prati, and F. Rocca (2000), Nonlinear subsidence rate estimation using permanent scatterers in differential SAR interferometry, *IEEE Trans. Geosci. Remote Sens.*, **38**, 2202–2212.
- Froger, J.-L., O. Merle, and P. Briole (2001), Active spreading and regional extension of Mount Etna imaged by SAR interferometry, *Earth Planet. Sci. Lett.*, **187**, 245–258.
- Hanssen, R. (2001), *Radar Interferometry*, Kluwer Acad., Norwell, Mass.
- Lanari, R., P. Lundgren, and E. Sansosti (1998), Dynamic deformation of Etna volcano observed by satellite radar interferometry, *Geophys. Res. Lett.*, **25**, 1541–1544.
- Lo Giudice, E., and R. Rasà (1992), Very shallow earthquakes and brittle deformation in active volcanic areas: The Etnan region as an example, *Tectonophysics*, **202**, 257–268.
- Lundgren, P., and P. A. Rosen (2003), Source model for the 2001 flank eruption of Mt. Etna volcano, *Geophys. Res. Lett.*, **30**(7), 1388, doi:10.1029/2002GL016774.
- Lundgren, P., S. Usai, E. Sansosti, R. Lanari, M. Tesauro, G. Fornaro, and P. Bernardino (2001), Modeling surface deformation observed with synthetic aperture radar interferometry at Campi Flegrei caldera, *J. Geophys. Res.*, **106**, 19,355–19,366.
- Lundgren, P., P. Bernardino, M. Coltelli, G. Fornaro, R. Lanari, G. Puglisi, E. Sansosti, and M. Tesauro (2003), Coupled magma chamber inflation and sector collapse slip observed with synthetic aperture radar interferometry on Mt. Etna volcano, *J. Geophys. Res.*, **108**(B5), 2247, doi:10.1029/2001JB000657.
- McGuire, W. J., I. S. Stewart, and S. J. Saunders (1997), Intra-volcanic rifting at Mount Etna in the context of regional tectonics, *Acta Vulcanol.*, **9**, 147–156.
- Merle, O., and A. Borgia (1996), Scaled experiments of volcano spreading, *J. Geophys. Res.*, **101**, 13,805–13,817.
- Patanè, D., P. De Gori, C. Chiarabba, and A. Bonaccorso (2003), Pressurization of Mount Etna's volcanic system, *Science*, **299**, 2061–2063.
- Rosen, P. A., S. Hensley, I. R. Joughin, F. K. Li, S. N. Madsen, E. Rodriguez, and R. M. Goldstein (2000), Synthetic aperture radar interferometry, *Proc. IEEE*, **88**, 333–382.
- Rust, D., and M. Neri (1996), The boundaries of large-scale collapse on the flanks of Mt. Etna, Sicily, in *Volcano Instability on the Earth and other Planets*, edited by W. J. McGuire, A. P. Jones, and J. Neuberg, *Geol. Soc. London Spec. Publ.*, **110**, 193–208.
- Tibaldi, A., and G. Groppelli (2002), Volcano-tectonic activity along structures of the unstable NE flank of Mt. Etna (Italy) and their possible origin, *J. Volcanol. Geotherm. Res.*, **115**, 277–302.

P. Berardino, F. Casu, R. Lanari, M. Manzo, A. Pepe, and E. Sansosti, IREA-CNR, Via Diocleziano, 328, 80124, Napoli, Italy. (berardino.p@irea.cnr.it; casu.f@irea.cnr.it; lanari.r@irea.cnr.it; manzo.mr@irea.cnr.it; pepe.a@irea.cnr.it; sansosti.e@irea.cnr.it)

P. Lundgren, Jet Propulsion Laboratory, California Institute of Technology, 4800 Oak Grove Drive, Pasadena, CA 91109, USA. (paul@weed.jpl.nasa.gov)